Dalton Transactions

ROYAL SOCIETY OF CHEMISTRY

PAPER

Published on 18 August 2023
Licence and permissions

Check for updates

Cite this: *Dalton Trans.*, 2023, **52**, 12347

Exposing high-activity (111) facet CoO octahedral loading MXene quantum dots for efficient and stable photocatalytic H_2 evolution †

Lan Ding, * Siyang Wang, Yaoyao Tang, Xinyi Chen and Hongjun Zhou*

Received 4th July 2023,
Accepted 3rd August 2023

DOI: 10.1039/d3dt02090h

rsc.li/dalton

Photocatalytic splitting of water for hydrogen generation is a green and renewable solution for converting solar energy to chemical energy; thus, the development of high-performance and stable photocatalytic materials has emerged as a research hotspot recently. Herein, a heterostructure composite photocatalyst of octahedral CoO uniformly modified with novel nitrogen-doped MXene quantum dots (N-MQDs) is successfully designed using a typical solvothermal approach. The optimum photocatalytic hydrogen evolution efficiency of the prepared N-MQDs@CoO heterojunction composite is 82.54 μmol g^{-1} h^{-1} with visible light, which is 16.57 times higher compared to the pure CoO. A series of photoelectrochemical tests were further performed to elucidate the photocatalytic hydrogen evolution mechanism. The remarkable improvement of activity is primarily attributed to the synergistic interaction between the closely spaced interface contacts and energy level matching among high conductivity Ti_3C_2 MXene quantum dots with CoO octahedra, dramatically hastening the segregation and transfer of photo-generated carriers. This study provides new ideas for the construction of MXene quantum dot-based co-photocatalysts with highly efficient photocatalytic performance and stability toward solar energy conversion applications.

1 Introduction

Solar energy is considered the most promising green renewable energy source for addressing the serious challenges of sustainable environment and energy depletion.[1–3] Photocatalytic water splitting technology for direct conversion of solar energy to hydrogen is considered to be an attractive and economically viable strategy.[4–6] Obviously, semiconductor-based composite photocatalytic materials are considered the most attractive candidate for generating carbon-free and renewable hydrogen energy in recent years.[7–9] Therefore, seeking low-consumption, environmentally friendly photocatalysts with excellent performance and high stability remains a central challenge today.

In recent years, cobalt monoxide (CoO) nanomaterials have emerged as a promising photocatalyst with a narrow visible light absorption band gap (2.6 eV) and remarkable solar-to-hydrogen conversion capability, as well as high economic efficiency and low production cost.[10–12] In addition, the CoO octahedral structure with the exposed (111) crystal plane has been demonstrated to produce hydrogen from water splitting under visible light irradiation.[13] However, the poor electron–hole separation ability generated by the photoexcitation of the octahedral CoO and easy deactivation of the (111) crystal plane during photocatalysis greatly inhibit its application in the field of catalysis. Various approaches, such as loading co-catalysts,[14] regulating the crystal surface,[15] and combination with other semiconductors,[16,17] have been explored to boost the photocatalytic hydrogen generation capacity of the octahedral CoO. Unfortunately, these methods can only appropriately enhance the photocatalytic hydrogen production performance of the materials, which was not conducive to improving the stability of the photocatalysts. Hence, improving the stability of the CoO octahedral (111) crystal plane and further enhancing the photocatalytic performance remains a challenging task. Notably, the combination of CoO with other novel materials to design heterojunctions can make sufficient use of the complementary advantages of each component to immensely separate photogenerated carriers, thus effectively boosting photocatalytic performance and photostability.[18,19] Therefore, exploring suitable strategies to successfully achieve the preparation of CoO-based heterojunction composites has become the current research hotspot.

Since Ti_3C_2 was discovered as a novel two-dimensional MXene layered material in 2011,[20] it has become a current hotspot for extensive research due to its good electronic

State Key Laboratory of Heavy Oil Processing Beijing Key Laboratory of Biogas Upgrading Utilization, China University of Petroleum-Beijing, Beijing 102249, China. E-mail: 15030527652@163.com

† Electronic supplementary information (ESI) available. See DOI: https://doi.org/10.1039/d3dt02090h

This journal is © The Royal Society of Chemistry 2023

conductivity, superior biocompatibility, and abundant active catalytic sites.[21–23] Quantum dots constructed from two-dimensional layer-like materials have distinctive properties compared to lamellar structures, for example, quantum restriction effects, optimal biocompatibility, superior modifiability of physicochemical characteristics, enriched reactive edge sites, and brilliant dispersion.[24–26] Furthermore, the edge architecture and extensive surface functional groups within MXene quantum dots facilitate the formation of heterojunctions to semiconductor materials, establishing strong built-in electric fields as well as tight interfacial contacts.[27,28] The synergistic effect can significantly hasten the transfer and separation of photo-generated electrons and holes in heterojunction contact interfaces, which is the key factor in improving photocatalytic performance. Recently, several studies have shown that the construction of heterojunctions of MXene quantum dots with Cu_2O, g-C_3N_4, and SiC significantly improved photocatalytic activity.[29–32]

In this work, a N-MQDs@CoO composite photocatalyst was successfully fabricated using a facile one-step solvothermal approach. Surprisingly, the synthesized novel heterojunction photocatalytic materials showed significantly higher efficiency in photocatalytic H_2 evolution upon visible light illumination, and the hydrogen generation performance was 16.57 times higher than pure octahedral CoO. Additionally, the N-MQDs@CoO-5% heterojunction material exhibits excellent photostability after five recycles of photocatalytic hydrogen production. The significant enhancement of photocatalytic performance and stability of the prepared N-MQDs@CoO composites was ascribed to the modification with N-MQDs, which dramatically improves the charge separation efficiency and the absorption of visible light, and effectively conducts the heat generated by the photothermal effect of CoO octahedra. The reasonable design and simple synthetic method of the composite is of significance not only for further enhancement of photocatalytic activity, but also for consolidating the stability of the CoO.

2 Experimental section

2.1 Synthetic method

Synthesis of layered Ti_3C_2 MXene. The two-dimensional layered material Ti_3C_2 MXene was successfully prepared *via* etching the precursor Ti_3AlC_2 phase using HF solution. Simply, 1.2 g Ti_3AlC_2 was thoroughly dissolved in 40 mL HF solution and stirred vigorously at room temperature and reacted for 72 h. The reacted mixture was centrifuged (8000 rpm) and washed repetitively with deionized water until the pH of the obtained supernatant reached 7, and the sample was then vacuum dried at 60 °C for 18 h.

Synthesis of Ti_3C_2 quantum dots (N-MQDs). Typically, 300 mg layered Ti_3C_2 MXene powder was dispersed in a mixture of concentrated nitric acid (15 mL) and concentrated sulfuric acid (45 mL) and stirred for 16 h in an oil bath (120 °C). The obtained solution was cooled naturally and then an appropriate amount of sodium hydroxide was added until the pH of the mixture reached 7. The nitrogen-doped Ti_3C_2 MXene quantum dots were further prepared through the typical hydrothermal method. 0.05 g melamine was added to 20 mL neutral Ti_3C_2 solution, sonicated vigorously for 20 min, and then transferred to a 50 mL Teflon reaction kettle, and reacted at 160 °C for 10 h. The cooled solution was filtered *via* a 25 mm × 0.22 μm PTFE membrane to eliminate the unreacted large particles. The solution was further purified with dialysis membranes, and deionized water was changed every 4–6 h until Na^+ was completely undetectable.

Synthesis of Ti_3C_2 sheets. 0.3 g Ti_3C_2 MXene was dispersed in 20 mL dimethyl sulfoxide (DMSO) solution, and vigorously sonicated for 36 h, followed by centrifugation at 7500 rpm for 0.5 h to eliminate the multilayer MXene and collect the monolayer Ti_3C_2 flakes. Finally, the sample was obtained by freeze-drying.

Synthesis of CoO and N-MQDs@CoO composites. The CoO octahedron photocatalyst was prepared by a typical solvothermal method. 1.84 g Co $(CH_3COO)_2{\cdot}4H_2O$ was dosed into a solvent mixture comprising 64 mL *n*-octanol and 16 mL ethanol. After 30 min of sufficient stirring, the resulting mixture was reacted in a 100 mL autoclave for 4 h at 220 °C. Finally, the obtained solution was repeatedly rinsed with ethanol and deionized water and vacuum dried overnight at 70 °C. For a series of N-MQDs@CoO composites, different mass percentages of N-MQDs were added during the preparation of CoO, respectively. The N-MQDs@CoO composites with different mass ratios of N-MQD powders (1 wt%, 3 wt%, 5 wt% and 7 wt%) were abbreviated as N-MQDs@CoO-1%, N-MQDs@CoO-3%, N-MQDs@CoO-5% and N-MQDs@CoO-7%, respectively.

2.2 Characterization

The crystal properties of the fabricated photocatalysts were evaluated using a Bruker D8 diffractometer under Cu-Kα radiation. Fourier transform infrared (FTIR) spectroscopy was performed utilizing Thermo Nicolet, Inc. instruments. The morphology was examined using Hitachi-S4800 *via* scanning electron microscopy (SEM) and JEOL-2100Fvia transmission electron microscopy (TEM). Time-resolved spectra and fluorescence spectra were attained on a Hitachi F-4500 fluorescence spectrophotometer. A Shimadzu UV-3600 spectrophotometer was employed for UV-visible diffuse reflectance (DRS) scanning with $BaSO_4$ as the reference. The chemical structure and bonding states were researched using X-ray photoelectron spectroscopy (XPS). The specific surface area was obtained by using the Brunauer–Emmett Teller model.

2.3 Photocatalytic hydrogen evolution experiment and photoelectrochemical test

The photocatalytic hydrogen production tests were conducted over a specific quartz reactor. In a classic experiment, 20 mg photocatalyst was dispersed in 100 mL of deionized water and magnetically stirred under vacuum. The temperature of the reaction solution was maintained at about 5 °C by circulating condensing equipment. The light generator is a 300 W Xe

 This journal is © The Royal Society of Chemistry 2023

lamp having irradiance (PLS-SXE300, PerfectLight). Gas chromatography (Fuli GC9790SD, TCD detector) was employed to determine the amount of hydrogen generated in the photocatalytic process. The photoelectrochemical measurements were performed at an electrochemical workstation (CHI760D, China). The synthesized N-MQDs@CoO and CoO powders were applied as working electrodes, Ag/AgCl served as the reference electrode and a platinum wire acted as the counter electrode. 0.1 M Na_2SO_4 was employed as the working electrolyte. The electrode was fabricated as follows: 15 mg powders were fully dispersed in a mixture of 950 μL anhydrous ethanol and 50 μL Nafion and vigorously sonicated for 20 min. The colloidal suspension was impregnated on an abluent ITO glass electrode and then vacuum dried for 10 h.

3 Results and discussion

The synthesis procedure for N-MQDs@CoO composite photocatalysts is presented (Fig. 1). Briefly, the layer-like Ti_3C_2 MXene structure was derived through selective etching of Al layers from the bulk Ti_3AlC_2 phase using HF solution. N-MQDs were fabricated *via* the hydrothermal treatment of layered Ti_3C_2 MXene. Finally, quantum dot modified CoO octahedral morphology samples were fabricated using a typical solvothermal approach. The morphology and structure of the synthesized materials were characterized through SEM, TEM, and AFM. The accordion-like multilayer Ti_3C_2 MXene was successfully derived by HF selective etching of Al layers (Fig. S1†). Elemental mapping of Ti_3C_2 MXene reveals the uniform distribution of C and Ti. Fig. 2a and Fig. S2† provide the TEM images of N-MQDs with a uniform size prepared by a simple hydrothermal method. The average particle diameter computed from the TEM image was 3.24 nm. HRTEM further examined the crystallographic structure of the as-prepared N-MQD sample, displaying clear lattice stripes with 0.266 nm, belonging to the (0110) crystal plane of layered Ti_3C_2 MXene. Fig. S3† presents the AFM images of N-MQDs analyzed for comparatively precise thicknesses. The average thickness for N-MQDs presents 1.06 nm, demonstrating that the majority of N-MQDs belong to monolayer quantum dots (Fig. S4†). Specifically, the prepared N-MQDs exhibit excellent optical properties attributed to the quantum size effect. Consequently, the optical properties of N-MQDs were sufficiently verified using fluorescence experiments. Fig. S5a† illustrates that the optimized excitation and emission wavelengths of the fluorescence spectra are 420 nm and 500 nm, respectively. Fig. S5b† indicates that the location and intensity of the emission peaks vary with the different excitation wavelengths, illustrating a distinct excitation-dependent PL behavior. Fig. S6† and Fig. 2b and c reveal the TEM images for pure CoO as ruled *ortho*-octahedral shapes. The exposed surface of the synthesized CoO octahedral structure is extremely smooth and displays strong (111)-selective orientation. TEM images of the N-MQDs@CoO composites revealed a huge amount of N-MQDs evenly distributed on the surface of CoO octahedra with tight interfacial contacts (Fig. 2d and e). The *in situ* coated N-MQDs on CoO did not disrupt the octahedral morphology but homogeneously dispersed on the surface, suggesting that the modification of N-MQDs did not influence the formation of CoO octahedra. The HRTEM image (Fig. 2f) showed distinct lattice stripes with 0.261 nm and 0.329 nm belonging to the (0110) and (111) facets of N-MQDs and CoO, respectively, evidencing that the *in situ* growth process does not detract from the crystallinity of the composite materials. The SAED image further demonstrates the coexistence of crystalline phases of N-MQDs and CoO in the composite (Fig. 2g). The elemental mapping for N-MQDs@CoO sufficiently evidences that the Ti, C, N, Co, and O elements were evenly distributed on the composites (Fig. 2h). These results indicate the tight interfacial connection between N-MQDs and CoO octahedra, which successfully constructs the electric field built into the heterojunction. Thus, the interfacial charge migration within the photocatalytic process is effectively promoted.

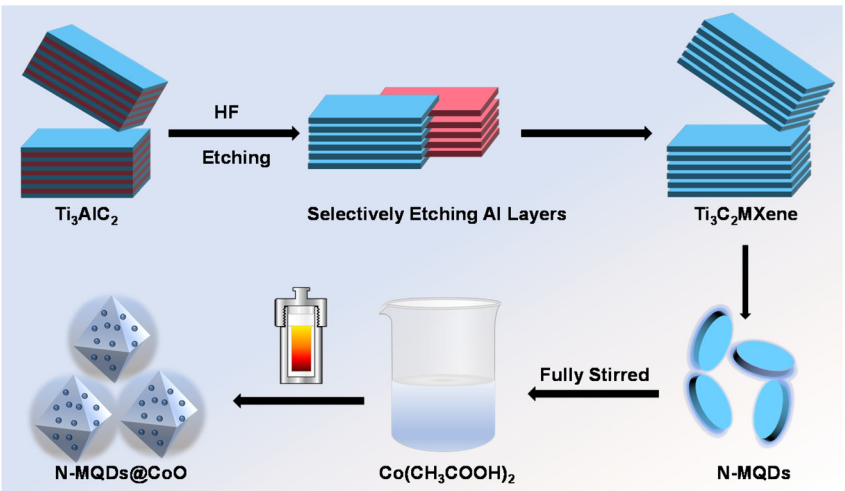

Fig. 1 The schematic illustration of the preparation process for the N-MQDs@CoO composite photocatalyst.

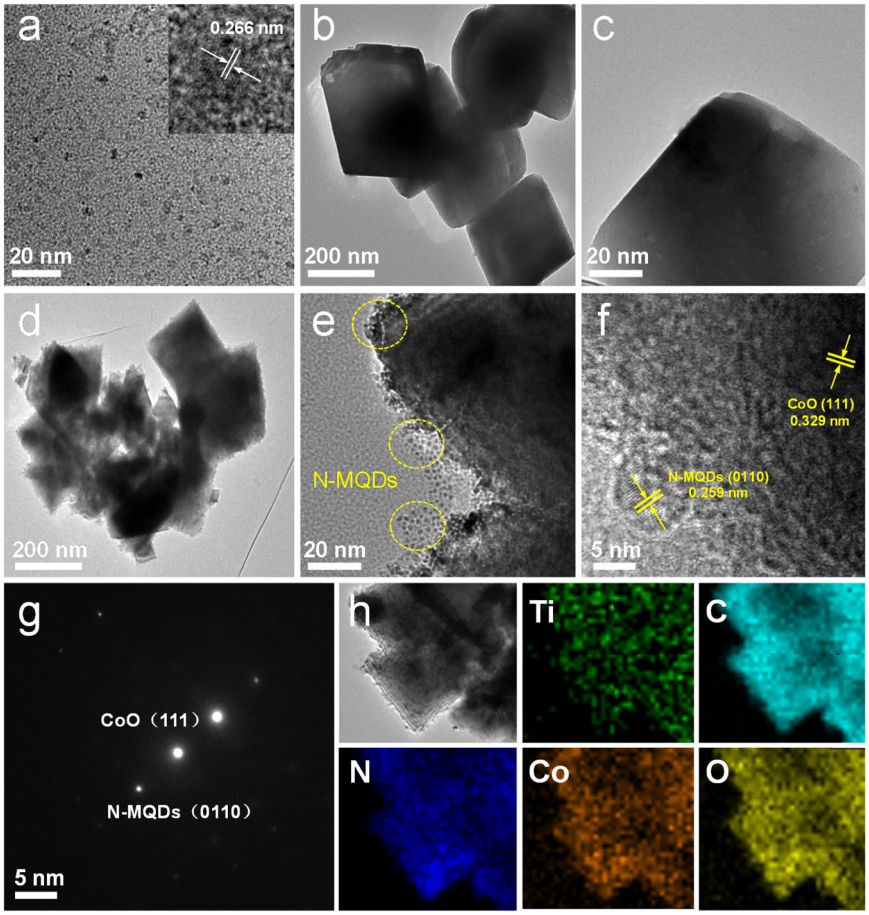

Fig. 2 (a) TEM and HRTEM images for N-MQDs. (b and c) TEM images for octahedral CoO. (d–f) TEM and HRTEM images for the as-prepared N-MQDs@CoO. (g) SEAD pattern for the N-MQDs@CoO photocatalyst. (h) Elemental mapping images for N-MQDs@CoO.

The crystalline structures for the various photocatalysts were evaluated *via* X-ray diffraction (XRD). As depicted in Fig. S7,† Ti_3AlC_2 displayed sharply defined peaks, agreeing with the prior research (JCPDS no. 52-0875).[33,34] After selective etching with HF solution, the diffraction peak vanished and the Ti_3C_2 MXene lamellar structure was shaped.[35] The broadening of the synthesized MXene layer spacing causes the typical peak (002) to weaken in intensity and shift to a lower location at 8.86°. The vanishing of the distinctive diffraction peak of 39° in Ti_3AlC_2 is further evidence of the effective elimination of the aluminum layer.[36] Moreover, N-MQDs remained detectable in the (002) and (004) crystal planes of the layer-like structure Ti_3C_2 MXene, demonstrating that the successfully fabricated quantum dots maintain partial chemical properties of the raw material. The distinctive diffraction peaks for pure CoO appearing at 36.5°, 42.4°, 61.6°, 73.8°, and 77.4° belong to the (111), (200), (220), (311), and (222) crystal planes for the face-centered cubic CoO structure (JCPDS no. 71-1178) (Fig. 3a).[37] The typical diffraction peaks of pristine CoO were observed in the N-MQDs@CoO composite photocatalyst and no obstruction peaks were established, suggesting that the modification with N-MQDs does not affect the crystallinity of CoO octahedra. Nevertheless, the absence of distinctive N-MQD characteristic diffraction peaks in the composites was assigned to the tiny content and complete distribution.[38,39] The Fourier transform infrared spectrum (FTIR) firmly established the decoration of N-MQDs upon the CoO octahedral surface (Fig. 3b). The strong peak towards 496 cm^{-1} and an apparent distinct shoulder near 632 cm^{-1} belong to the stretching vibrations of Ti–C and Ti–O, which is consistent with Ti 2p XPS, demonstrating that N-MQDs maintain the skeletal structure with Ti_3C_2 MXene.[40,41] The intense peaks near 1529 cm^{-1} and 1378 cm^{-1} are classified as interior vibrations of N–H bonds and C–N stretching vibrations, suggesting the successful doping of N elements within the quantum dots.[42,43] The stretching vibrational peaks of Co–O and O–H appeared at 440 cm^{-1} and 3430 cm^{-1} with pure octahedral CoO.[44] The FTIR spectra for the N-MQDs@CoO photocatalyst revealed the vibrational peaks corresponding to both CoO and N-MQDs, demonstrating the successful coupling of N-MQDs to CoO and the preservation of the intact CoO structural skeleton. Furthermore, the pore size distribution and specific surface area of the fabricated photocatalysts were evaluated utilizing N_2 adsorption–desorption isotherms (Fig. 3c and d). The

 This journal is © The Royal Society of Chemistry 2023

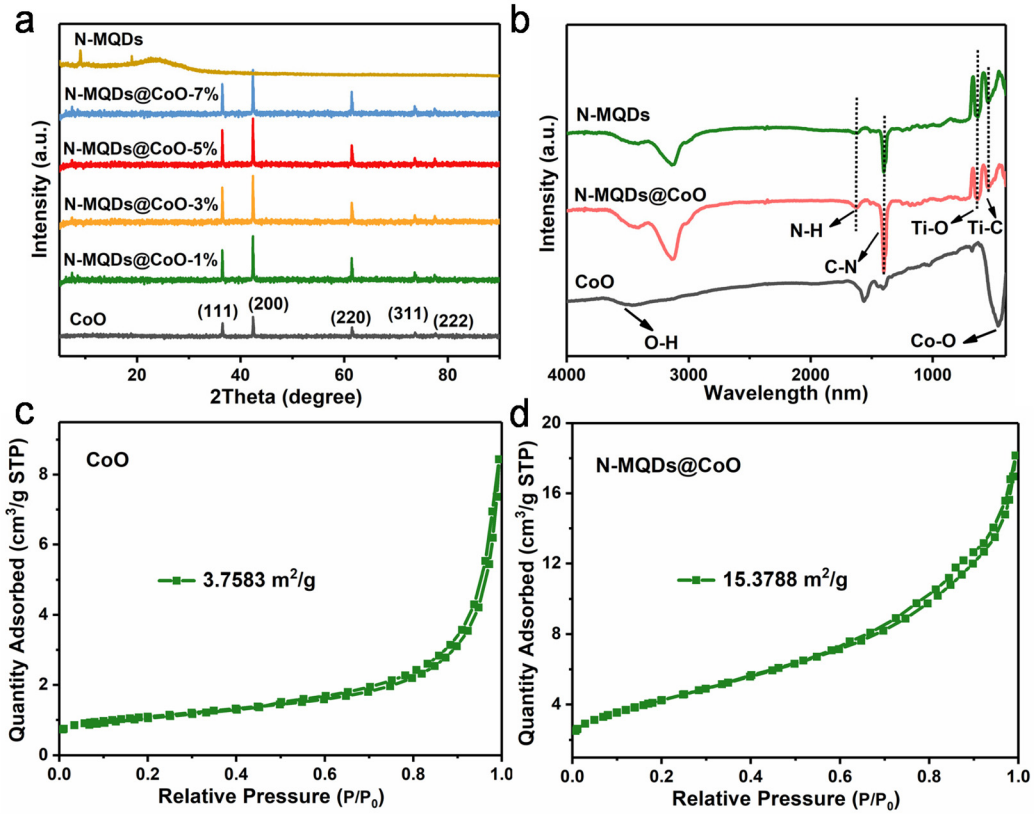

Fig. 3 (a) XRD pattern and (b) FT-IR spectroscopy for N-MQDs, CoO, and N-MQDs@CoO. (c and d) N_2 adsorption–desorption isotherms and BET for CoO and N-MQDs@CoO.

specific surface area of the N-MQDs/CoO composite photocatalyst (15.37 $m^2\ g^{-1}$) was substantially greater than that of pure CoO (3.75 $m^2\ g^{-1}$), illustrating that the combination with N-MQDs could remarkably boost the specific surface area of octahedral CoO, offering more catalytic active sites and further strengthening the photocatalytic hydrogen production performance.

The chemical components and bonding states for the fabricated samples were evaluated using X-ray photoelectron spectroscopy (XPS). The XPS survey spectrum (Fig. 4a) indicates that Co and O elements were present in pure CoO. In comparison, Ti and N elements were identified among the N-MQDs@CoO, demonstrating that the N-MQDs successfully distributed on the CoO octahedral surface, which is consistent with the EDX elemental mapping findings. Fig. 4b displays the Ti 2p spectra for N-MQDs@CoO showing five peaks belonging to the Ti–C bond (461.6 and 454.8 eV), Ti–N bond (456.3 eV) and Ti–O peak (464.6 and 458.8 eV),[45,46] indicating that the appearance of the Ti–N peak confirms the presence of N element among Ti_3C_2 MXene quantum dots. Simultaneously, the N 1s spectrum (Fig. 4c) presents three peaks centered at 397.3 eV, 398.4 eV, and 399.5 eV, accordingly belonging to the newly formed Ti–N peak, pyridine N, and pyrrole N, fully substantiating the introduction of nitrogen.[47–49] The C 1s XPS spectrum for pure CoO (Fig. S8†) exhibits peaks near 284.7 eV, 288.8 eV, and 286.1 eV, corresponding to the C–C/C═C, C–O, and C═O bonds.[50] In comparison with pure CoO, the prepared N-MQDs@CoO composite photocatalyst showed an additional peak near 283.5 eV assigned to the C–Ti bond (Fig. 4d), further evidence for the effective composite of N-MQDs and CoO. The high-resolution Co 2p spectra for CoO (Fig. 4e) display two predominant peaks near the binding energies of 781.2 eV and 796.8 eV, coupled to two distinct satellite peaks corresponding to inherent Co^{2+} oxidation states Co $2p_{3/2}$ and Co $2p_{1/2}$ orbitals among the CoO phases.[51,52] The Co 2p spectra of N-MQDs@CoO shifted to higher binding energy (0.58 eV) compared with the pristine CoO, fully evidencing the electron transfer from CoO toward N-MQDs and the strong interfacial interactions. The phenomenon is ascribed to the unique heterojunction-induced quick separation of photogenerated carriers. Consequently, the constructed N-MQDs@CoO can significantly restrain the photo-generated carrier recombination and boost the carrier transfer efficiency. In addition, the high-resolution XPS O 1s spectra for CoO and N-MQDs@CoO (Fig. 4f) exhibit two typical peaks at 529.3 and 531.3 eV positions, representing the Co–O and Co–O–C bonds within the CoO phase.[53,54]

The photocatalytic hydrogen generation behaviors of the prepared series of photocatalysts under visible light were investigated. The comparative experiments in Fig. S10† revealed no H_2 production in the absence of light and photocatalyst and

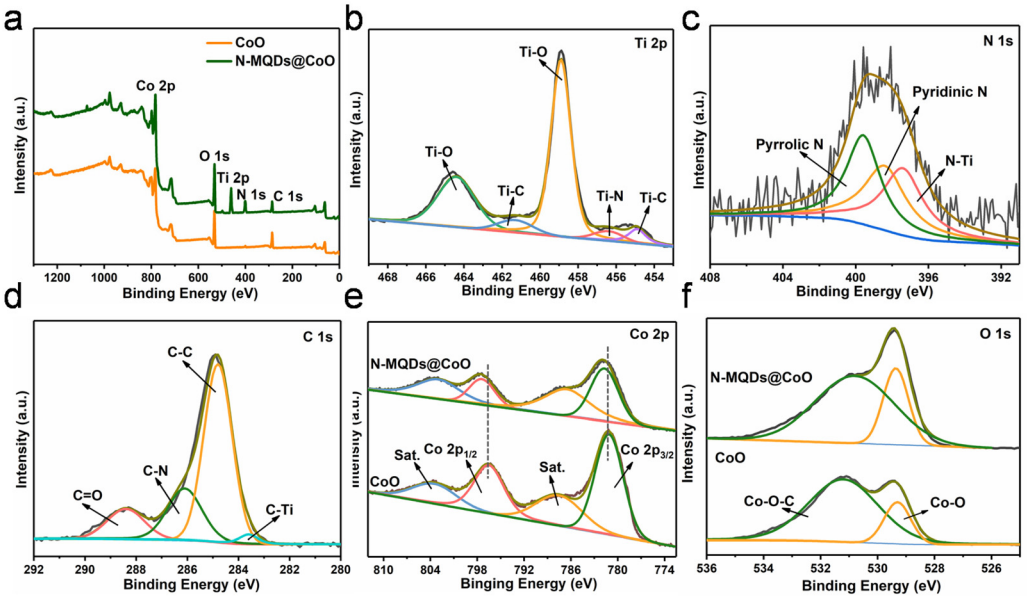

Fig. 4 (a) XPS survey for pure CoO and N-MQDs@CoO. (b–d) Ti 2p, N 1s and C 1s XPS for N-MQDs@CoO. (e) Co 2p XPS for pure CoO and N-MQDs@CoO. (f) O 1s XPS for CoO and N-MQDs@CoO.

pure N-MQDs without hydrogen production capacity. As shown in Fig. 5a and b, the pure CoO octahedra themselves exhibit relatively inferior photogenerated carrier separation, leading to rapid recombination of charges and restricted efficiency of photocatalytic H_2 generation (4.98 μmol g^{-1} h^{-1}). Surprisingly, the hydrogen generation capacity of N-MQDs/CoO loaded with N-MQDs is extremely enhanced, reaching 82.54 μmol h^{-1} g^{-1} with visible light. The H_2 production

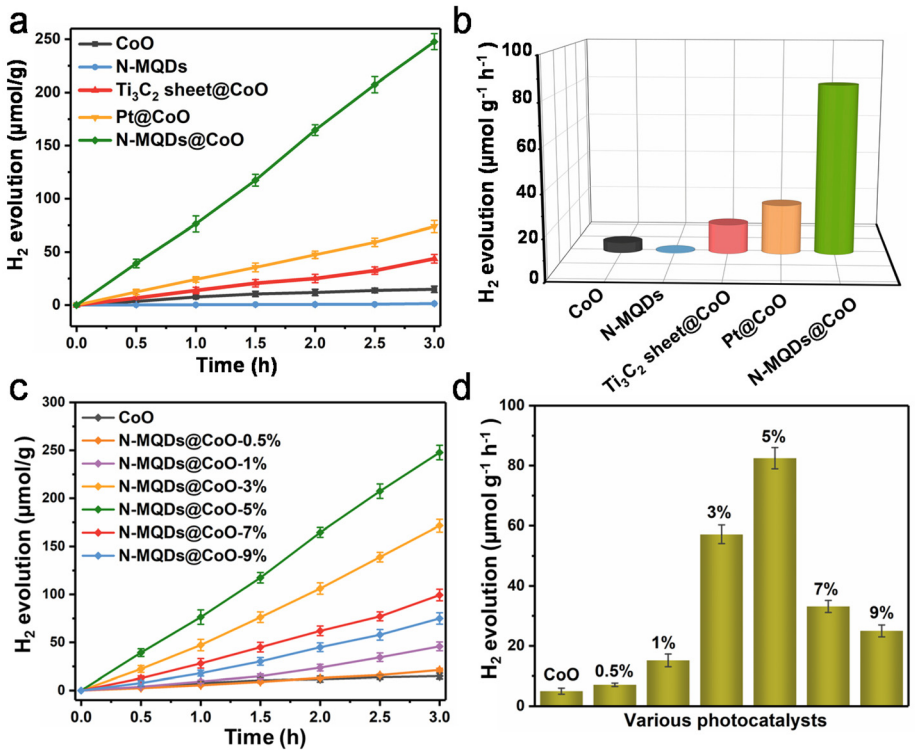

Fig. 5 (a) Photocatalytic H_2 production capacity of the synthetic series of photocatalysts with visible light illumination. (b) Photocatalytic H_2 generation rate of different samples. (c and d) The H_2 evolution performance of N-MQDs@CoO loaded with various N-MQD contents upon visible light illumination.

This journal is © The Royal Society of Chemistry 2023

efficiency of the optimized N-MQDs@CoO composite photocatalyst is 16.57 times higher than that of pure CoO. Fig. S11† presents the three-dimensional gas chromatogram for the N-MQDs@CoO composite photocatalyst used in hydrogen production. The characteristic peak with hydrogen evolution (detention time = 2.23 min) was distinctly detected to significantly increase with longer reaction time. Moreover, the H_2 production rate of N-MQDs@CoO was nearly 3.35 times and 5.67 times higher than that of Pt/CoO (24.63 μmol g^{-1} h^{-1}) and Ti_3C_2 MXene flakes/CoO (14.57 μmol g^{-1} h^{-1}). These above experimental findings demonstrate that MXene quantum dots provide dramatic benefits compared favorably with other materials in enhancing photocatalytic hydrogen generation. Table S3† illustrates that the constructed N-MQDs@CoO is the superior catalyst in terms of hydrogen generation capability among such materials compared to the recently reported CoO-based composites. The efficient photocatalytic activity of N-MQDs@CoO is mainly attributed to the conductive MXene quantum dots as electron acceptors and the synergistic effect of the built-in electric field that accelerates the transfer and separation of photogenerated charges. To obtain the optimized heterojunction photocatalyst, the loading of different N-MQD ratios on octahedral CoO was explored. The experiments in Fig. 5c and d demonstrated that the photocatalytic H_2 generation efficiency of N-MQDs@CoO samples increased accordingly upon continuously rising N-MQD incorporation. The hydrogen generation capacity of the N-MQDs@CoO composite photocatalyst reached the highest when the N-MQD loading was 5%. However, the efficiency of photocatalytic hydrogen production for the N-MQDs@CoO composites decreases continuously as the N-MQD content increases from 5% to 9%. The result is attributed to the aggregation phenomenon due to the increased loading of N-MQDs, which inhibits the absorption of visible light from CoO. In addition, abundant N-MQDs act as photoinduced recombination centers for electrons and holes, thus reducing photocatalytic activity.

In addition, the photocatalytic stability of the fabricated N-MQDs/CoO composites was evaluated through cycling hydrogen production performance experiments. Fig. 6a indicates that the hydrogen production efficiency of pure CoO decreased significantly during four consecutive photocatalytic processes, and the hydrogen rate of the N-MQDs@CoO composite photocatalyst was basically stable, demonstrating the excellent stability of N-MQDs@CoO. The XRD, TEM, and UV of the N-MQDs@CoO samples after the H_2 evolution reaction proved that neither characteristic diffraction peaks change (Fig. 6b, c and Fig. S12†), nor structural destruction and the light absorption capacity did not decrease, indicating that the synthesized composite photocatalysts possess excellent structural and photostability. The above results further demonstrate that the modification of functionalized N-MQDs enables CoO to prevent localized overheating deactivation and greatly improves photocatalytic performance.

To further evidence the transfer mode of photoexcited carriers in composite photocatalysts, photocurrent response, polarization curves (LSV curves), and EIS were evaluated. Fig. 7a illustrates the instantaneous photocurrent response of CoO and N-MQDs@CoO. Compared with pure CoO, the photocurrent intensity of N-MQDs@CoO-5% is significantly increased, demonstrating substantially enhanced charge separation and superior photo responsiveness. The advantageous carrier separation efficiency is attributed to the availability of N-MQDs to accept photogenerated electrons transferred from CoO, favoring the quick separation of electrons and holes. Electrochemical impedance spectroscopy (EIS) proved to be a crucial tool to investigate the charge transfer manner. The fitted equivalent circuit was designed as shown in the inset of Fig. 7b. R_s and R_{ct} denote the series resistance and charge transfer resistance. The results show that the EIS Nyquist radius of N-MQDs@CoO is smaller than that of pure CoO. The fitted electrochemical impedance (Table S1†) indicated that the charge transfer resistance for the N-MQDs@CoO photocatalyst was merely 4.48 Ω, which was considerably less than that of pure CoO (27.72 Ω). The reduction in charge transfer resistance suggests that the contact surface exhibits favorable charge transmission and separation capability. The LSV curves (Fig. 7c) further identified the photocurrent density and water splitting initiation potential of the as-prepared samples.[55] The experiments revealed that the photocurrent density of the N-MQDs@CoO composite photocatalyst was remarkably higher than that of the CoO sample, suggesting that the visible light collection was enhanced upon the N-MQD modification of CoO. In addition, the water splitting initiation potential of N-MQDs@CoO-5% is −260 mV (*vs.* NHE), significantly smaller than that of CoO (−490 mV *vs.* NHE), demonstrating that the loading of N-MQDs facilitates the photocatalytic hydrogen production reaction. The frequency peak for the prepared working electrode of N-MQDs@CoO is reduced from 53.28 Hz to 8.64 Hz in comparison to pure CoO (Fig. S13†). The peak transfer between higher and lower frequencies reveals faster electron transfer procedures since the frequency (f) is intimately linked with the lifetime of the infused electrons (τ), which is 6.17 times longer than that of pure CoO according to the equation $\tau \approx 1/(2\pi f)$, suggesting that the infused electron lifetime for N-MQDs@CoO is dramatically higher, which markedly blocks the electron–hole recombination. The optical absorption behavior of CoO and N-MQDs@CoO-5% was evaluated through UV-vis diffuse reflectance. From Fig. 7d, the pure CoO displays a remarkable absorption from the UV into the visible area, manifesting a band gap absorption edge near 490 nm. Most fundamentally, the absorption capacity of N-MQDs@CoO composites in the visible region was strengthened upon loading of N-MQDs, demonstrating that N-MQDs enhance the visible light acquisition efficiency, facilitating the improvement of photocatalytic hydrogen evolution performance. Fig. 7e presents the PL spectra for pure CoO and N-MQDs/CoO photocatalysts. CoO exhibits a distinct emission peak nearby 580 nm, induced by the photoexcited carrier recombination. The PL intensity of the N-MQDs@CoO photocatalyst decreased dramatically upon the increment of N-MQD loading, displaying superior photoinduced hole and electron

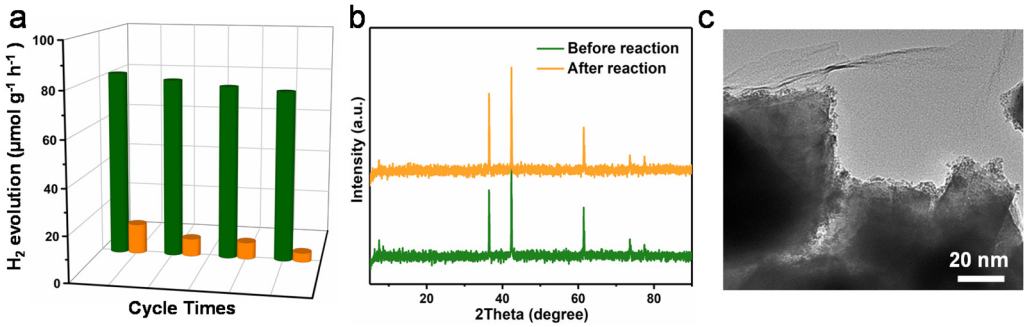

Fig. 6 (a) Photocatalytic cycle hydrogen production activity measurements for CoO and N-MQDs@CoO with visible light illumination. (b and c) XRD and TEM images for N-MQDs@CoO after the multi-cycle photocatalytic process.

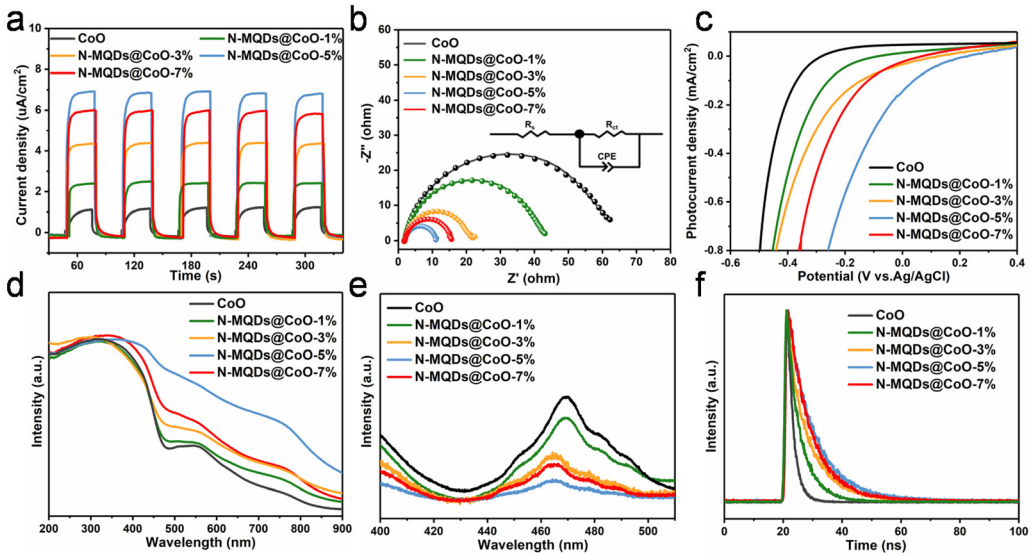

Fig. 7 (a) Photocurrent profiles and (b) electrochemical impedance plots for CoO and N-MQDs@CoO samples. (c) LSV profiles for pure CoO and N-MQDs@CoO. (d) UV-vis absorption spectra for CoO and N-MQDs@CoO composite photocatalysts. (e) Fluorescence spectra for CoO and N-MQDs@CoO samples. (f) Time-resolved PL decay spectra for CoO and N-MQDs@CoO corresponding to the steady-state emission peaks.

separation capability. Simultaneously, the fluorescence lifetime of the samples was characterized using time-resolved fluorescence decay spectra. Longer lifetimes imply less recombination and higher reaction probability. Fig. 7f reveals that the lifetime (τ) for the N-MQDs@CoO photocatalyst is 8.43 ns, significantly higher compared with the CoO (2.19 ns), further suggesting that the electric field built into the heterojunction constructed by N-MQDs and CoO suppresses the recombination of photo-generated carriers. Therefore, the lifetime of the carriers involved in the photocatalytic hydrogen generation reaction is extended after the loading of N-MQDs, which improves their possibility to participate in the photocatalytic reaction before the recombination for the N-MQDs@CoO heterojunction. In addition, we added the surface photovoltage (SPV) experiment to the revised manuscript (Fig. S13†). The surface photovoltage directly confirms the accumulation state of photogenerated charges on the surface. Notably, the N-MQDs@CoO exhibited a pronounced stronger SPV response intensity compared with pure CoO. Since the stronger SPV signal represents the higher carrier separation efficiency, the charge transfer process at the heterojunction interface was very effective and favorable to the electron leap of CoO. The above-discussed experimental findings demonstrate that the N-MQDs@CoO composite photocatalysts exhibit outstanding charge separation and transfer efficiency driven by the strong interfacial electric field, resulting in superior visible-light-driven hydrogen production performance.

The energy band position of the photocatalyst determines the charge transfer mode and action mechanism in the photocatalytic procedure. The Kubelka–Munk equation (Fig. 8a) was employed to compute the appropriate forbidden bandwidths according to the UV-Vis spectra. The band gap of pure CoO is 2.5 eV, whereas the band gap of N-MQDs@CoO is significantly reduced to 2.41 eV, suggesting that the introduction of N-MQDs facilitates the photocatalyst to harvest visible light and enhance visible light absorption. The Mott–Schottky

 This journal is © The Royal Society of Chemistry 2023

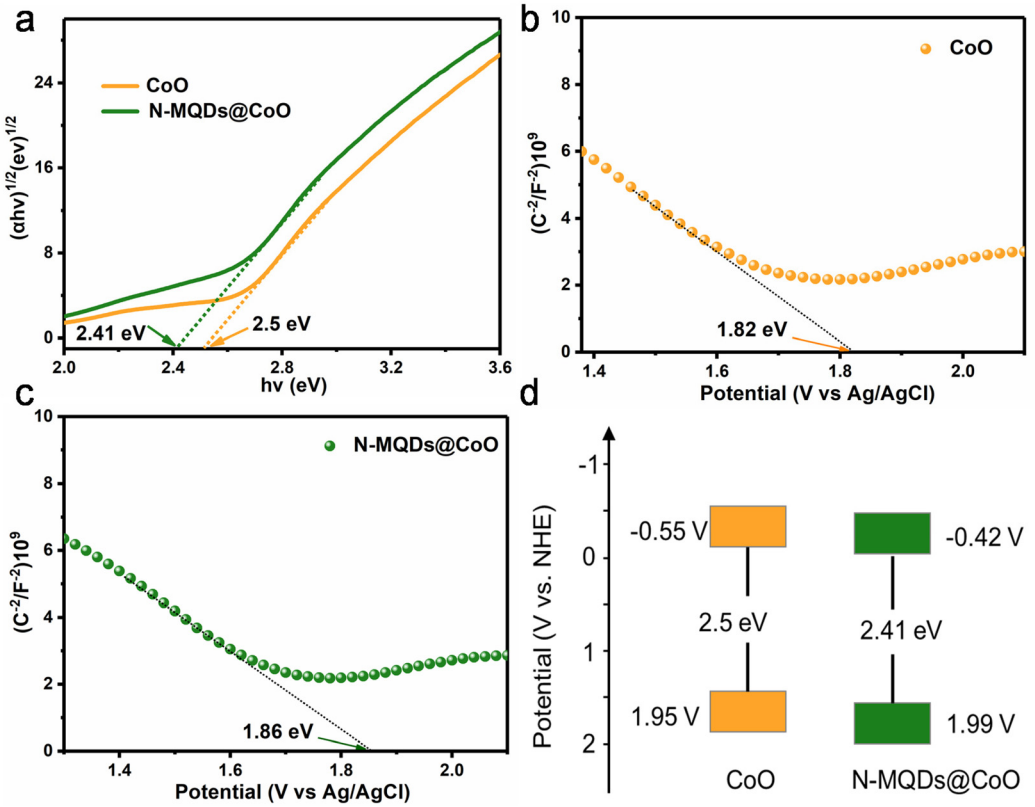

Fig. 8 (a) Kubelka–Munk parameter conversion for CoO and N-MQDs@CoO. (b and c) Mott–Schottky plots for CoO and N-MQDs@CoO. (d) Energy band structure alignments for CoO and N-MQDs@CoO.

curves (Fig. 8b and c) of the prepared samples were evaluated using photoelectric measurements. The negative slope of $1/C^2$ (C is the capacitance) *versus* the imposed potential reveals that pure CoO is a classic p-type semiconductor material. The carrier densities (N_d) of the samples can be calculated from the Mott–Schottky equation.[56,57]

$$N_d = \frac{2}{(e_0\varepsilon\varepsilon_0)[d/(1/C^2)/dV]^{-1}}$$

where e_0 is the electron charge (1.6×10^{-19} C), ε is the dielectric constant of CoO, ε_0 is the vacuum dielectric constant (8.86×10^{-12} F m^{-1}), and V is the applied bias at the electrode. N-MQDs@CoO (6.39×10^{23} cm^{-3}) can be seen to exhibit the higher carrier density than pure CoO (4.25×10^{23} cm^{-3}), indicating a faster charge transfer and a higher donor density, which results in an enhanced PEC performance. Furthermore, the flat-band (fb) edge position for p-type semiconductors is 0.1–0.3 eV less compared to the valence band (E_{VB}) edge position.[58] The fb values of pure CoO and N-MQDs@CoO were computed to be 1.82 eV and 1.86 eV *vs.* Ag/AgCl, respectively. Thus, the E_{VB} positions of CoO and N-MQDs@CoO are 1.95 eV and 1.99 eV. The significant shift in fb potential demonstrates that the closely contacted interface through CoO with N-MQDs creates a built-in electric field, which dramatically facilitates electron transport across the octahedral CoO toward N-MQDs. According to the formula ($E_g = E_{VB} - E_{CB}$), the conduction bands for pure CoO and N-MQDs@CoO are identified to be −0.55 eV and −0.42 eV. The diagram of the energy band positions for octahedral CoO and N-MQDs@CoO is depicted in Fig. 8d.

Based on the above-mentioned findings, the probable mechanism underlying the photocatalytic splitting of water in N-MQDs@CoO heterojunction composites was presented, as shown in Fig. 9. Since the Fermi energy level of CoO is different from that of N-MQDs, when CoO and N-MQDs are in close contact, the electrons are spontaneously transferred from N-MQDs to CoO through the interface until the Fermi level achieves a new equilibrium. It follows that an interfacial electric field is generated at the contact interface. The octahedral CoO is photoexcited to form electrons and holes in the composite photocatalyst system under visible light illumination. Due to the excellent electron transfer properties of N-MQDs and the constructed heterojunction built-in electric field, the electrons generated in CoO can be freely transferred to the inside of N-MQDs for photocatalytic hydrogen evolution reactions, and the holes are retained inside the valence band with CoO, thereby effectively suppressing the photoexcited electron–hole recombination and further enhancing the photocatalytic activities for CoO. In addition, owing to the photothermal effect in the photocatalytic process, N-MQDs as heat conductors can remove the surface heat of octahedral CoO to obviate CoO deactivation.

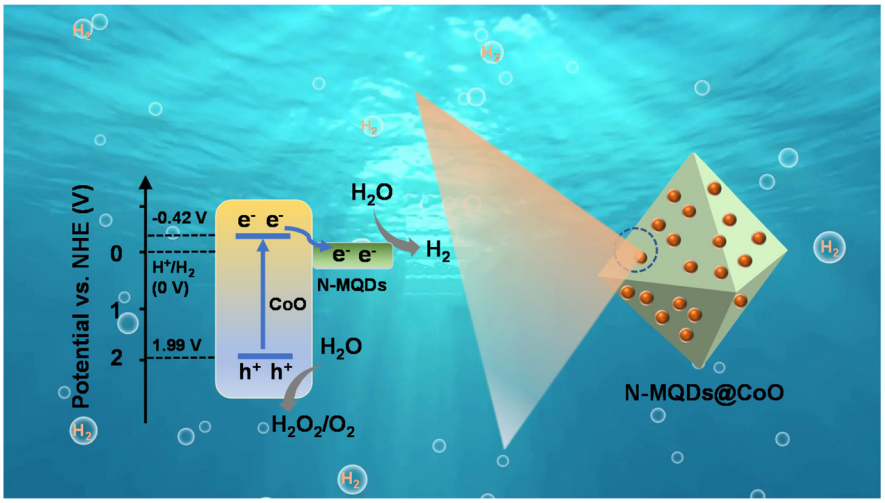

Fig. 9 Mechanism illustration of H_2 evolution of the N-MQDs@CoO heterojunction photocatalyst under visible light.

4 Conclusions

In summary, a novel N-MQDs@CoO nanohybrid heterojunction photocatalytic material was prepared using a typical solvothermal strategy; namely, the octahedral CoO surface was modified with the homogeneous size MXene quantum dots by *in situ* growth. The photocatalytic hydrogen production activity results revealed that the optimized N-MQDs@CoO photocatalyst exhibits remarkable photocatalytic ability with a photocatalytic hydrogen efficiency of 82.54 μmol h^{-1} g^{-1}, which is 16.57 times higher compared with pure CoO. The superior photocatalytic efficiency with N-MQDs@CoO photocatalysts can be attributed to the tight interfacial contact between MXene quantum dots and CoO and the driving force of the built-in electric field. At the heterojunction interface for N-MQDs@CoO, the interfacial electric field directed from N-MQDs to CoO dramatically promotes the electron transfer from the conduction band of CoO to the electron acceptor of N-MQDs, which can subsequently participate in the H_2 generation reaction. Thus, the constructed heterojunction can help to suppress the recombination of photogenerated carriers and achieve efficient interfacial charge transfer separation, thus significantly improving the capacity of the interfacial H_2 evolution reaction. This research presents novel insights for the application of MXene quantum dots in photocatalysis and expands the design strategy for the preparation of an efficient photocatalyst for water splitting.

Conflicts of interest

There are no conflicts of interest to declare.

Acknowledgements

This research was supported by the Foundation of China University of Petroleum, Beijing (No. 2462019BJRC007, 2462020YXZZ018) and the National Natural Science Foundation of China (No. 5211101820).

References

1 M. Han, C. Y. Kang, Z. X. Qu, S. J. Zhu and B. Yang, Surface molecule induced effective light absorption and charge transfer for H_2 production photocatalysis in a carbonized polymer dots-carbon nitride system, *Appl. Catal., B*, 2022, **305**, 121064.

2 Y. X. Shi, Q. Zhao, J. Y. Li, G. Y. Gao and J. F. Zhi, Onion-liked carbon-embedded graphitic carbon nitride for enhanced photocatalytic hydrogen evolution and dye degradation, *Appl. Catal., B*, 2022, **308**, 121216.

3 F. Gao, Y. Zhao, L. L. Zhang, B. Wang, Y. Z. Wang, X. Y. Huang, K. Q. Wang, W. H. Feng and P. Liu, Well dispersed MoC quantum dots in ultrathin carbon films as efficient co-catalysts for photocatalytic H_2 evolution, *J. Mater. Chem. A*, 2018, **6**, 18979–18986.

4 T. Yan, X. J. Zhang, H. Liu and Z. L. Jin, CeO_2 Particles Anchored to Ni_2P Nanoplate for Efficient Photocatalytic Hydrogen Evolution, *Chin. J. Struct. Chem.*, 2022, **41**, 2201047–2201053.

5 F. S. Xing, R. Y. Zeng, C. C. Cheng, Q. W. Liu and C. J. Huang, POM-incorporated $ZnIn_2S_4$ Z-scheme dual-functional photocatalysts for cooperative benzyl alcohol oxidation and H_2 evolution in aqueous solution, *Appl. Catal., B*, 2022, **306**, 121087.

6 Y. J. Dong, Q. Han, Q. Y. Hu, C. J. Xu, C. Z. Dong, Y. Peng, Y. Ding and Y. Q. Lan, Carbon quantum dots enriching molecular nickel polyoxometalate over CdS semiconductor for photocatalytic water splitting, *Appl. Catal., B*, 2021, **293**, 120214.

7 J. C. Xu, W. Zhong, D. D. Gao, X. F. Wang, P. Wang and H. G. Yu, Phosphorus-enriched platinum diphosphide nanodots as a highly efficient cocatalyst for photocatalytic H_2 evolution of CdS, *Chem. Eng. J.*, 2022, **439**, 135758.

 This journal is © The Royal Society of Chemistry 2023

8 Z. L. Wang, L. X. Wang, B. Cheng, H. G. Yu and J. G. Yu, Photocatalytic H_2 Evolution Coupled with Furfuralcohol Oxidation over Pt-Modified ZnCdS Solid Solution, *Small Methods*, 2021, **5**, 2100979.

9 B. W. He, C. B. Bie, X. G. Fei, B. Cheng, J. G. Yu, W. K. Ho, A. A. Al-Ghamdi and S. Wageh, Enhancement in the photocatalytic H_2 production activity of CdS NRs by Ag_2S and NiS dual cocatalysts, *Appl. Catal., B*, 2021, **288**, 119994.

10 L. B. Liao, Q. H. Zhang, Z. H. Su, Z. Z. Zhao, Y. N. Wang, Y. Li, X. X. Lu, D. G. Wei, G. Y. Feng, Q. K. Yu, X. J. Cai, J. M. Zhao, Z. F. Ren, H. Fang, F. Robles-Hernandez, S. Baldelli and J. Bao, Efficient solar water-splitting using a nanocrystalline CoO photocatalyst, *Nat. Nanotechnol.*, 2014, **9**, 69–73.

11 L. He, W. Y. Zhang, S. Liu and Y. Zhao, Three-dimensional porous N-doped graphitic carbon framework with embedded CoO for photocatalytic CO_2 reduction, *Appl. Catal., B*, 2021, **298**, 120546.

12 X. M. Xu, L. J. Meng, J. Luo, M. Zhang, Y. T. Wang, Y. X. Dai, C. Sun, Z. Y. Wang, S. G. Yang, H. He and S. B. Wang, Self-assembled ultrathin CoO/Bi quantum dots/defective Bi_2MoO_6 hollow Z-scheme heterojunction for visible light-driven degradation of diazinon in water matrix: Intermediate toxicity and photocatalytic mechanism, *Appl. Catal., B*, 2021, **293**, 120231.

13 W. L. Shi, F. Guo, H. B. Wang, S. J. Guo, H. Li, Y. Zhou, C. Zhu, Y. J. Liu, H. Huang, B. D. Mao, Y. Liu and Z. H. Kang, New Insight of Water-Splitting Photocatalyst: H_2O_2-Resistance Poisoning and Photothermal Deactivation in Sub-micrometer CoO Octahedrons, *ACS Appl. Mater. Interfaces*, 2017, **9**, 20585–20593.

14 F. Guo, X. L. Huang, Z. H. Chen, H. R. Sun and L. Z. Chen, Anchoring CoP nanoparticles on the octahedral CoO by self-phosphating for enhanced photocatalytic overall water splitting activity under visible light, *Chin. J. Chem. Eng.*, 2021, **40**, 114–123.

15 B. Liu, L. Ma, L. C. Ning, C. J. Zhang, G. P. Han, C. J. Pei, H. Zhao, S. Z. Liu and H. Q. Yang, Charge Separation between Polar {111} Surfaces of CoO Octahedrons and Their Enhanced Visible-Light Photocatalytic Activity, *ACS Appl. Mater. Interfaces*, 2015, **7**, 6109–6117.

16 W. L. Shi, F. Guo, C. Zhu, H. B. Wang, H. Li, H. Huang, Y. Liu and Z. H. Kang, Carbon dots anchored on octahedral CoO as a stable visible-light-responsive composite photocatalyst for overall water splitting, *J. Mater. Chem. A*, 2017, **5**, 19800–19807.

17 W. L. Shi, F. Guo, M. Y. Li, Y. Shi, M. J. Shi and C. Yan, Constructing 3D sub-micrometer CoO octahedrons packed with layered MoS_2 shell for boosting photocatalytic overall water splitting activity, *Appl. Surf. Sci.*, 2019, **473**, 928–933.

18 Z. L. Jin, H. Y. Li and J. K. Li, Efficient photocatalytic hydrogen evolution over graphdiyne boosted with a cobalt sulfide formed S–scheme heterojunction, *Chin. J. Catal.*, 2022, **43**, 303–315.

19 S. Bera, S. Ghosh, T. Maiyalagan and R. N. Basu, Band Edge Engineering of $BiOX/CuFe_2O_4$ Heterostructures for Efficient Water Splitting, *ACS Appl. Energy Mater.*, 2022, **5**, 3821–3833.

20 Y. Xia, T. S. Mathis, M. Q. Zhao, B. Anasori, A. Dang, Z. Zhou, H. Cho, Y. Gogotsi and S. Yang, Thickness-independent capacitance of vertically aligned liquid-crystalline MXenes, *Nature*, 2018, **557**, 409–412.

21 Y. C. Dong, S. S. K. Mallineni, K. Maleski, H. Behlow, V. N. Mochalin, A. M. Rao, Y. Gogotsi and R. Podila, Metallic MXenes: A new family of materials for flexible triboelectric nanogenerators, *Nano Energy*, 2018, **44**, 103–110.

22 A. D. Dillon, M. J. Ghidiu, A. L. Krick, J. Griggs, S. J. May, Y. Gogotsi, M. W. Barsoum and A. T. Fafarman, Highly Conductive Optical Quality Solution-Processed Films of 2D Titanium Carbide, *Adv. Funct. Mater.*, 2016, **26**, 4162–4168.

23 S. Y. Lu, L. Z. Sui, J. J. Liu, S. J. Zhu, A. M. Chen, M. X. Jin and B. Yang, Near-Infrared Photoluminescent Polymer-Carbon Nanodots with Two-Photon Fluorescence, *Adv. Mater.*, 2017, **29**, 1603443.

24 C. Xia, Y. R. Qiu, Y. Xia, P. Zhu, G. King, X. Zhang, Z. Y. Wu, J. Y. Kim, D. A. Cullen, D. X. Zheng, P. Li, M. Shakouri, E. Heredia, P. X. Cui, H. N. Alshareef, Y. F. Hu and H. T. Wang, General synthesis of single-atom catalysts with high metal loading using graphene quantum dots, *Nat. Chem.*, 2021, **13**, 887–894.

25 W. Zhai, T. F. Xiong, Z. He, S. Y. Lu, Z. C. Lai, Q. Y. He, C. L. Tan and H. Zhang, Nanodots Derived from Layered Materials: Synthesis and Applications, *Adv. Mater.*, 2021, **33**, 2006661.

26 S. C. Chen, C. Y. Lin, T. L. Cheng and W. L. Tseng, 6-Mercaptopurine-Induced Fluorescence Quenching of Monolayer MoS_2 Nanodots: Applications to Glutathione Sensing, Cellular Imaging, and Glutathione-Stimulated Drug Delivery, *Adv. Funct. Mater.*, 2017, **27**, 1702452.

27 R. Nag, P. Bhakuni, S. R. Barman and A. Bera, MXene as a Superior Charge-Transport Layer in an MXene-$BiFeO_3$-ZnO Nanocomposite for Photocatalytic Disintegration of Antacids, *ACS Appl. Eng. Mater.*, 2023, **1**, 1034–1047.

28 Y. J. Yuan, L. Jiang, X. Li, P. Zuo, X. Q. Zhang, Y. L. Lian, Y. L. Ma, M. S. Liang, Y. Zhao and L. T. Qu, Ultrafast Shaped Laser Induced Synthesis of MXene Quantum Dots/Graphene for Transparent Supercapacitors, *Adv. Mater.*, 2022, **34**, 2110013.

29 Z. P. Zeng, Y. B. Yan, J. Chen, P. Zan, Q. H. Tian and P. Chen, Boosting the Photocatalytic Ability of Cu_2O Nanowires for CO_2 Conversion by MXene Quantum Dots, *Adv. Funct. Mater.*, 2019, **29**, 1806500.

30 Y. J. Li, L. Ding, Y. C. Guo, Z. Q. Liang, H. Z. Cui and J. Tian, Boosting the Photocatalytic Ability of g-C_3N_4 for Hydrogen Production by Ti_3C_2 MXene Quantum Dots, *ACS Appl. Mater. Interfaces*, 2019, **11**, 41440–41447.

31 B. B. Chang, Y. Z. Guo, H. L. Liu, L. Li and B. C. Yang, Engineering a surface defect-rich Ti_3C_2 quantum dots/mesoporous C_3N_4 hollow nanosphere Schottky junction for efficient N_2 photofixation, *J. Mater. Chem. A*, 2022, **10**, 3134–3145.

32 H. M. Wang, R. Zhao, H. X. Hu, X. W. Fan, D. Zhang and D. J. Wang, 0D/2D Heterojunctions of Ti_3C_2 MXene QDs/SiC as an Efficient and Robust Photocatalyst for Boosting the Visible Photocatalytic NO Pollutant Removal Ability, *ACS Appl. Mater. Interfaces*, 2020, **12**, 40176–40185.

33 A. Jawaid, A. Hassan, G. Neher, D. Nepal, R. Pachter, W. J. Kennedy, S. Ramakrishnan and R. A. Vaia, Halogen Etch of Ti_3AlC_2 MAX Phase for MXene Fabrication, *ACS Nano*, 2021, **15**, 2771–2777.

34 T. S. Mathis, K. Maleski, A. Goad, A. Sarycheva, M. Anayee, A. C. Foucher, K. Hantanasirisakul, C. E. Shuck, E. A. Stach and Y. Gogotsi, Modified MAX Phase Synthesis for Environmentally Stable and Highly Conductive Ti_3C_2 MXene, *ACS Nano*, 2021, **15**, 6420–6429.

35 Y. Liao, J. Qian, G. Xie, Q. Han, W. Q. Dang, Y. S. Wang, L. L. Lv, S. Zhao, L. Luo, W. Zhang, H. Y. Jiang and J. W. Tang, 2D-layered Ti_3C_2 MXenes for promoted synthesis of NH_3 on P25 photocatalysts, *Appl. Catal., B*, 2020, **273**, 119054.

36 C. J. Lu, L. Yang, B. Z. Yan, L. B. Sun, P. G. Zhang, W. Zhang and Z. M. Sun, Nitrogen-Doped Ti_3C_2 MXene: Mechanism Investigation and Electrochemical Analysis, *Adv. Funct. Mater.*, 2020, **30**, 2000852.

37 P. J. Guo, Z. Y. Xiong, S. Y. Yuan, K. H. Xie, H. J. Wang and Y. J. Gao, The synergistic effect of Co/CoO hybrid structure combined with biomass materials promotes photocatalytic hydrogen evolution, *Chem. Eng. J.*, 2021, **420**, 130372.

38 Q. Wang, J. S. Cai, G. V. Biesold-McGee, J. Y. Huang, Y. H. Ng, H. T. Sun, J. P. Wang, Y. K. Lai and Z. Q. Lin, Silk fibroin-derived nitrogen-doped carbon quantum dots anchored on TiO_2 nanotube arrays for heterogeneous photocatalytic degradation and water splitting, *Nano Energy*, 2020, **78**, 105313.

39 H. W. Lv, R. J. Sa, P. Y. Li, D. Q. Yuan, X. C. Wang and R. H. Wang, Metalloporphyrin-based covalent organic frameworks composed of the electron donor-acceptor dyads for visible-light-driven selective CO_2 reduction, *Sci. China: Chem.*, 2020, **63**, 1289–1294.

40 Z. Guo, X. H. Zhu, S. G. Wang, C. Y. Lei, Y. Huang, Z. Nie and S. Z. Yao, Fluorescent Ti_3C_2 MXene quantum dots for an alkaline phosphatase assay and embryonic stem cell identification based on the inner filter effect, *Nanoscale*, 2018, **10**, 19579–19585.

41 Y. N. Jiang, T. Sun, X. Xie, W. Jiang, J. Li, B. B. Tian and C. L. Su, Oxygen-Functionalized Ultrathin $Ti_3C_2T_x$ MXene for Enhanced Electrocatalytic Hydrogen Evolution, *ChemSusChem*, 2019, **12**, 1368–1373.

42 Y. Li, Y. Zhao, J. Wu, Y. D. Han, H. Huang, Y. Liu and Z. H. Kang, Photo-charge regulation of metal-free photocatalyst by carbon dots for efficient and stable hydrogen peroxide production, *J. Mater. Chem. A*, 2021, **9**, 25453–25462.

43 T. Y. Cheng, F. P. Chou, S. C. Huang, C. Y. Chang and T. K. Wu, Electroluminescence and photocatalytic hydrogen evolution of S,N co-doped graphene oxide quantum dots, *J. Mater. Chem. A*, 2022, **10**, 3650–3658.

44 F. Guo, W. L. Shi, C. Zhu, H. Li and Z. H. Kang, CoO and g-C_3N_4 complement each other for highly efficient overall water splitting under visible light, *Appl. Catal., B*, 2018, **226**, 412–420.

45 J. F. Ding, C. Tang, G. J. Zhu, W. W. Sun, A. J. Du, F. Y. He, M. H. Wu and H. J. Zhang, Integrating SnS_2 Quantum Dots with Nitrogen-Doped $Ti_3C_2T_x$ MXene Nanosheets for Robust Sodium Storage Performance, *ACS Appl. Energy Mater.*, 2021, **4**, 846–854.

46 Z. D. Fan, C. H. Wei, L. H. Yu, Z. Xia, J. S. Cai, Z. N. Tian, G. F. Zou, S. X. Dou and J. Y. Sun, 3D Printing of Porous Nitrogen-Doped Ti_3C_2 MXene Scaffolds for High-Performance Sodium-Ion Hybrid Capacitors, *ACS Nano*, 2020, **14**, 867–876.

47 Y. Wang, L. Chen, H. T. Liu, Z. M. Xiong, L. Zhao, S. H. Liu, C. M. Huang and Y. M. Zhao, Cornlike ordered N-doped carbon coated hollow Fe_3O_4 by magnetic self-assembly for the application of Li-ion battery, *Chem. Eng. J.*, 2019, **356**, 746–755.

48 Z. H. Yan, Z. Y. Huang, H. H. Zhou, X. X. Yang, S. L. Li, W. L. Zhang, F. Wang and Y. F. Kuang, Facile fabrication of MoP nanodots embedded in porous carbon as excellent anode material for potassium-ion batteries, *J. Energy Chem.*, 2021, **54**, 571–578.

49 W. X. Yang, J. H. Zhou, S. Wang, W. Y. Zhang, Z. C. Wang, F. Lv, K. Wang, Q. Sun and S. J. Guo, Freestanding film made by necklace-like N-doped hollow carbon with hierarchical pores for high-performance potassium-ion storage, *Energy Environ. Sci.*, 2019, **12**, 1605–1612.

50 J. Z. Guo, Y. S. Lu, A. Q. Xie, G. Li, Z. B. Liang, C. F. Wang, X. N. Yang and S. Chen, Yellow-Emissive Carbon Dots with High Solid-State Photoluminescence, *Adv. Funct. Mater.*, 2022, **32**, 2110393.

51 K. Chen, S. Zhou, T. T. Jiang, X. D. Li, J. Yu, Q. Y. Wang, X. L. Xu and L. X. Zhu, Synergy of Fe dopants and oxygen vacancies confined in atomically-thin cobaltous oxide sheets for high-efficiency CO_2 photoreduction, *J. Mater. Chem. A*, 2021, **9**, 22353–22363.

52 K. Ma, F. Liu, Y. F. Yuan, X. Q. Liu, J. Wang, J. Xie and J. P. Cheng, CoO microspheres and metallic Co evolved from hexagonal α-$Co(OH)_2$ plates in a hydrothermal process for lithium storage and magnetic applications, *Phys. Chem. Chem. Phys.*, 2018, **20**, 595–604.

53 Z. B. Fan, X. Guo, M. X. Yang and Z. L. Jin, Mechanochemical preparation and application of graphdiyne coupled with CdSe nanoparticles for efficient photocatalytic hydrogen production, *Chin. J. Catal.*, 2022, **43**, 2708–2719.

54 Y. Cao, H. Q. Gou, P. F. Zhu and Z. L. Jin, Ingenious Design of CoAl-LDH p-n Heterojunction Based on CuI as Holes Receptor for Photocatalytic Hydrogen Evolution, *Chin. J. Struct. Chem.*, 2022, **41**, 2206079–2206085.

55 S. Q. Gong, J. C. Fan, V. Cecen, C. P. Huang, Y. L. Min, Q. J. Xu and H. M. Li, Noble-metal and cocatalyst free W_2N/C/TiO photocatalysts for efficient photocatalytic

 This journal is © The Royal Society of Chemistry 2023

overall water splitting in visible and near-infrared light regions, *Chem. Eng. J.*, 2021, **405**, 126913.
56 T. X. Ma, C. M. Yang, L. Guo, R. A. Soomro, D. J. Wang, B. Xu and F. Fu, Refining electronic properties of Bi_2MoO_6 by In-doping for boosting overall nitrogen fixation via relay catalysis, *Appl. Catal., B*, 2023, **330**, 122643.
57 Q. L. Ma, R. Song, F. J. Ren, H. Wang, W. S. Gao, Z. L. Li and C. Li, Photoelectrocatalytic degradation of refractory pollutants over WO_3/W network photoelectrode with heterophase junction for enhancing mass transportation and charge separation, *Appl. Catal., B*, 2022, **309**, 121292.
58 K. Chen, S. Zhou, T. T. Jiang, X. D. Li, J. Yu, Q. Y. Wang, X. L. Xu and L. X. Zhu, Synergy of Fe dopants and oxygen vacancies confined in atomically-thin cobaltous oxide sheets for high-efficiency CO_2 photoreduction, *J. Mater. Chem. A*, 2021, **9**, 22353–22363.

This journal is © The Royal Society of Chemistry 2023